Applied Surface Science 479 (2019) 1057–1067

Contents lists available at ScienceDirect

Applied Surface Science

journal homepage: www.elsevier.com/locate/apsusc

Full length article

A DFT study and microkinetic analysis of CO oxidation to dimethyl oxalate over Pd stripe and Pd single atom-doped Cu(111) surfaces

Bingying Han[a], Lixia Ling[b,c,d,*], Maohong Fan[c], Ping Liu[d], Baojun Wang[a,*], Riguang Zhang[a]

[a] Key Laboratory of Coal Science and Technology of Ministry of Education and Shanxi Province, Taiyuan University of Technology, Taiyuan 030024, PR China
[b] College of Chemistry and Chemical Engineering, Taiyuan University of Technology, Taiyuan 030024, PR China
[c] Department of Chemical and Petroleum Engineering, University of Wyoming, 1000 E University Ave, Laramie, WY 82071, USA
[d] State Key Laboratory of Coal Conversion, Institute of Coal Chemistry, Chinese Academy of Sciences, Taiyuan 030001, PR China

ARTICLE INFO

Keywords:
Pd_4Cu_8/Cu(111)
Pd_1-Cu(111)
CO oxidation to DMO
DFT
Microkinetic analysis
Activity

ABSTRACT

Developing low amount and high catalytic performance of Pd-based catalysts are vital for the oxidation of CO to dimethyl oxalate (DMO) in industry. In this study, Pd stripe and Pd single atom-doped Cu(111) surfaces are constructed via Pd substituting four striped Cu atoms and single Cu atom of surface layer over the Cu(111) surface, respectively, namely Pd_4Cu_8/Cu(111) and Pd_1-Cu(111) surfaces, and two possible reaction pathways related to DMO synthesis have been studied on two surfaces employing density functional theory (DFT) calculation in combination with microkinetic analysis and subsequently compared with the cases of Pd(111) and Pd_{ML}/Cu(111). The results show that $COOCH_3$-$COOCH_3$ coupling pathway is superior to $COOCH_3$-CO on Pd_4Cu_8/Cu(111) and Pd_1-Cu(111). Moreover, the Pd_1-Cu(111) surface shows highest catalytic activity for DMO generation, followed by the Pd_4Cu_8/Cu(111), the Pd(111) and the Pd_{ML}/Cu(111) surface. Additionally, Pd_4Cu_8/Cu(111) and Pd_1-Cu(111) surfaces exhibit high DMO selectivity. Thus, Pd stripe and Pd single atom-doped Cu(111) surfaces are thought to be prospective candidates to improve the catalytic performance of noble Pd and reduce its usage for CO oxidation to DMO.

1. Introduction

Dimethyl oxalate (DMO, $(COOCH_3)_2$), as an important chemical raw material, is widely applied in preparing pharmaceuticals, dyes, solvent, oxalic acid, and ethylene glycol (EG) [1–6], etc. The traditional synthesis method of DMO is mainly oxidative carbonylation of CH_3OH, CO and O_2 in the liquid-phase using $PdCl_2$-$CuCl_2$ catalysts [7]. However, this process is carried out under high pressure, and the condition is harsh. In addition, the catalyst is susceptible to deactivation due to metal poisoning or leaching, and liquid phase system is easy to corrode equipment. In recent decades, synthesis of DMO by the gas phase method was developed and increasingly prosperous. Unstable substance of methyl nitrite (CH_3ONO, MN) is introduced in the gas phase method and it easily decomposes into OCH_3 and NO [8–10], then two OCH_3 radicals can be oxidatively coupled with two CO to produce DMO on Pd-based catalysts [11–13], which is described by the equation: $2CO + 2CH_3ONO \rightarrow (COOCH_3)_2 + 2NO$. Meanwhile, the produced NO directly desorbs [14] and rapidly reacts with O_2 and CH_3OH to complete the regeneration of CH_3ONO in the absence of any catalyst [15–18], which is shown in the equation: $2NO + 2CH_3OH + 1/2O_2 \rightarrow 2CH_3ONO + H_2O$. The first chemical reaction can be proceeded at 0.1–0.5 Mpa and 375–415 K [19], and the second can be carried out under ambient temperature [17]. Therefore, the gas-phase method is widely adopted to produce DMO owing to moderate reaction conditions and low energy consumption.

Pd is the only metal confirmed to be excellent catalytic activity, selectivity and stability for DMO synthesis by gas-phase method and its (111) plane is demonstrated to be the main active facet for DMO formation [19]. However, the scarcity and expensive price of Pd metal as well as high Pd usage of an industrial catalyst hamper its large-scale and sustainable industrial applications [20,21]. Thus, how to reduce the usage of noble Pd meanwhile maintain high catalytic performance is the key to our research.

Pd-based bimetallic catalysts that cheaper metal substrates are doped by a trace amount of Pd atoms can be as a strategy to lower Pd usage and enhance the catalytic performance [22–31]. The Cu, as a low-cost metal, is considered to be a fine support for preparation of the Pd-doped Cu bimetallic catalyst with remarkable catalytic performance. Cai et al. [32] synthesized carbon-supported Cu@CuPd core-shell catalysts through the galvanic replacement approach and compared their

* Corresponding authors at: No. 79 West Yingze Street, Taiyuan University of Technology, Taiyuan 030024, PR China.
E-mail addresses: linglixia@tyut.edu.cn (L. Ling), wangbaojun@tyut.edu.cn (B. Wang).

https://doi.org/10.1016/j.apsusc.2019.02.112
Received 14 December 2018; Received in revised form 22 January 2019; Accepted 12 February 2019
Available online 14 February 2019
0169-4332/

catalytic performance for ethanol oxidation with those of the most advanced Pd/C and PdCu/C catalysts, it was found that Cu@CuPd/C catalysts showed higher catalytic activity and durability. Additionally, Cu nanotube decorated by PdCu nanoparticle was prepared via a facile seed-mediated growth approach and its catalytic activity for the formic acid oxidation was about 3.4 and 1.7 times better than those of Pd/C and PdCuNPs/C catalysts, which validated the results of previous DFT prediction [33]. More recently, Pd_1−Cu single-atom alloy catalysts that Cu substrates are doped by isolated, individual Pd atoms, have attracted tremendous attention owing to its extraordinary catalytic performance and maximum Pd atom utilization efficiency [34–49]. Experimentally, individual Pd atom doped in Cu(111) surface has been fabricated by chemical vapor deposition method and it exhibited more supreme catalytic activity for H_2 dissociation than Pd monolayer supported on Cu substrate or pure Pd [50]. An another important example of Cu-alloyed Pd single atoms nanoparticles were synthesized by galvanic replacement, where a small amount of Pd atoms were isolatedly doped onto the surface of Cu nanoparticles, and it showed more excellent catalytic activity toward phenylacetylene hydrogenation in contrast to either monometallic catalyst [51]. Besides, the Pd_1−Cu single-atom alloy catalyst was fabricated through the incipient wetness coimpregnation approach and its catalytic performance toward acetylene semihydrogenation was significantly superior to that of either monometallic [52].

It is known that different amounts of Pd atoms from monolayer to single atom deposited on the Cu(111) surface have been successfully prepared by using vapor deposition method or galvanic replacement [32,50]. And, previous work showed Pd monolayer-doped the Cu(111) surface, i.e. Pd_{ML}/Cu(111) surface, exhibited a slightly lower catalytic activity toward DMO synthesis as compared to the case on the Pd(111) surface, but interestingly, DMO synthesis mainly occurred on striped Pd atoms of surface layer on the Pd_{ML}/Cu(111) surface [12]. Additionally, the catalytic performance of Pd single atom-doped Cu(111) surface toward DMO formation is also unclear and remains to be studied. Nowadays, theoretical calculation based on density functional theory (DFT) with microkinetic analysis has played as an important role in designing novel catalysts [53–65]. Based on this, Pd stripe and Pd single atom-doped Cu(111) surfaces, namely Pd_4Cu_8/Cu(111) and Pd_1-Cu (111) surfaces, are constructed via Pd replacing four striped Cu atoms and single Cu atom of surface layer over the Cu(111) surface, respectively, and investigated toward DMO synthesis, which are compared with the cases of Pd_{ML}/Cu(111), to simulate the catalytic performance of different amounts of Pd atoms doped on Cu(111) surfaces in experiment. It is anticipated that the results of this work can help rationally design low-cost and high catalytic performance Pd-based bimetallic catalysts.

Additionally, one metal doped on another metal substrate can give rise to strain effect that refers to stress compression or tension caused by substrate metal toward doped metal and ligand effect that arises from charge transfer between doped metal and substrate metal, resulting in unique catalytic performance of bimetallic catalysts [66–75]. Zhang et al. [66] investigated CO oxidation on Au-doped Pd(111), and found that appropriate amount of Au atoms could promote the reaction of CO oxidation, which was ascribed to weak strain effect and strong ligand effect. However, how the strain and ligand affect DMO generation on Pd_4Cu_8/Cu(111) and Pd_1-Cu(111) is still unknown and remains to be elucidated.

2. Computational methods and models

All periodic density functional theory (DFT) calculations about CO oxidation to DMO were implemented within the VASP (Vienna Ab-initio Software Package) [76–78]. Projector-augmented wave (PAW) pseudopotentials was adopted to depict electron-ion interaction [79–81]. The exchange-correlation functional has been depicted by Perdew-Burke-Ernzerhof (PBE) [82] within the generalized gradient approximation (GGA). A (3 × 2 × 1) Monk-horst-Pack k-point mesh was employed in the Brillouin zone sampling. The plane wave being 400 eV cutoff energy was set to expand the electronic wave functions. Self-consistent iteration during the geometry optimizations were converged until forces and electronic energy on the unconstraint atoms were less than 0.03 eV·Å^{-1} force difference and 1×10^{-5} eV energy change. The transition states (TSs) of each elementary reaction about DMO formation were searched to obtain the favorable reaction path. Firstly, the image which was close to the structure of transition state was located through the climbing-image nudged elastic band (CI-NEB) method [83,84]. Then, it was relaxed again via using the dimer approach [85,86] until the atomic force was smaller than 0.05 eV/Å and finally verified by frequency analysis. All electronic energies are corrected by the zero point energy (ZPE): $ZPE = \sum_{i=1} \frac{hvi}{2}$ (1), where h and ν_i refer to the Planck constant and the calculated real frequency, respectively. The reaction energy (ΔE) and activation energy (E_a) can be obtained via the following formulas: $\Delta E = E_{FS} - E_{IS}$ (2) and $E_a = E_{TS} - E_{IS}$ (3), where E_{FS} stands for the energy of final state, E_{IS} refers to that of initial state, as well as E_{TS} represents that of transition state. The harmonic transition state theory (TST) [87] has been employed into calculating the rate constant for each reaction step: $k = \frac{k_B T}{h} \frac{\prod_{i=1}^{3N}\left[1-\exp\left(-\frac{h\nu_i^{IS}}{k_B T}\right)\right]}{\prod_{i=1}^{3N-1}\left[1-\exp\left(-\frac{h\nu_i^{TS}}{k_B T}\right)\right]} \exp\left(\frac{-E_a}{RT}\right)$ (4), where k_B and T stand for Boltzmann constant and the temperature. In addition, ν_i^{IS} and ν_i^{TS} stand for the real vibrational frequencies in the initial and transition states, respectively.

In this work, the lattice parameters (3.955 and 3.623 Å) of optimized bulk Pd and Cu by DFT well agree with the experimentally observed values (3.900 [88] and 3.615 Å [89]). The pure Cu(111) surface is firstly built by using a p(3 × 4) unit cell containing three-metal layers, then four striped Cu atoms and single Cu atom of surface layer are replacing with Pd atoms to represent Pd stripe and Pd single atom-doped Cu(111) surfaces, i.e. Pd_4Cu_8/Cu(111) and Pd_1-Cu(111), ultimately their supercells are optimized. This method was adopted to build Pd_{ML}/M(111) surfaces (M = Co, Ni, Cu, Al) with three-atomic-layer [11,12]. Meanwhile, the vacuum region of 10 Å is adopted in order to avoid the influence of the periodically repeated slabs. During the calculations, the upper two layers and the adsorbed species are permitted to relax while bottom one layer remains frozen. (See Fig. 1.)

To confirm the sufficiency of the selected cutoff energy (400 eV) and k-point mesh (3 × 2 × 1), we firstly compare the adsorption energies of CO on the Pd top site over Pd_4Cu_8/Cu(111) and Pd_1-Cu(111) surfaces at the cutoff energy of 400 eV with those at the cutoff energy of 450 and 500 eV, respectively. The results show that the corresponding adsorption energies are −87.0, −84.8 and −85.7 kJ/mol on the Pd_4Cu_8/Cu (111) surface, −101.2, −99.0 and −99.8 kJ/mol on the Pd_1-Cu(111) surface, implying that the adsorption energy does not change very much when the cutoff energy is beyond 400 eV. Then, the adsorption energy of CO with the k-point mesh (3 × 2 × 1) is compared with those at the k-point mesh of 4 × 3 × 1 and 5 × 4 × 1, respectively, indicating that the corresponding adsorption energies are −87.0, −84.5 and −87.9 kJ/mol on the Pd_4Cu_8/Cu(111) surface, −101.2, −98.4 and −102.1 kJ/mol on the Pd_1-Cu(111) surface, which implies that there has little influence on the same catalysts when k-point mesh increases (see Table 1). Therefore, considering the calculation efficiency, the selected cutoff energy (400 eV) and k-point mesh (3 × 2 × 1) are thought to be enough and suitable for our calculated systems.

Additionally, to demonstrate the selected p(3 × 4) supercell and three-layer model are sufficient for our calculated system, the adsorption energy of CO at the Pd top site on p(3 × 4) supercell model is firstly compared with those on p(4 × 4) and p(4 × 5) supercell, respectively, which are −87.0, −84.6 and −88.4 kJ/mol on the Pd_4Cu_8/Cu(111) surface, −101.2, −98.7 and −100.6 kJ/mol on the Pd_1-Cu (111) surface, implying that the adsorption energy does not change

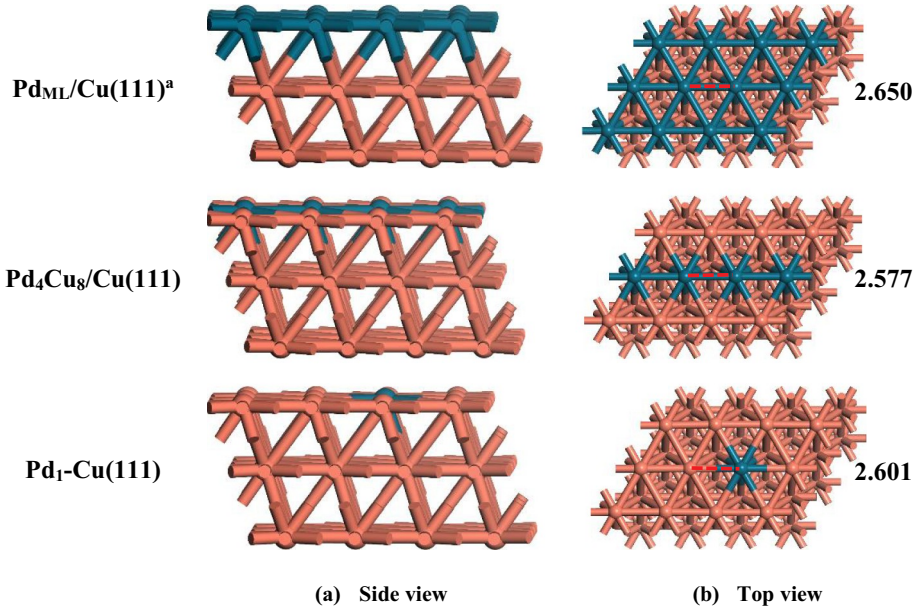

Fig. 1. The configurations of Pd_4Cu_8/Cu(111) and Pd_1-Cu(111) surfaces; (a, b) side and top view. Dark cyan and orange balls stand for Pd and Cu, respectively. [a] The study in Ref. [12].

Table 1
Test results about the effect of cut-off energy and k-point mesh on the adsorption energy (kJ/mol) of CO at the Pd top site over Pd_4Cu_8/Cu(111) and Pd_1-Cu(111) surfaces.

	Cut-off energy			K-point mesh		
	400 eV	450 eV	500 eV	3 × 2 × 1	4 × 3 × 1	5 × 4 × 1
Pd_4Cu_8/Cu(111)	−87.0	−84.8	−85.7	−87.0	−84.5	−87.9
Pd_1-Cu(111)	−101.2	−99.0	−99.8	−101.2	−98.4	−102.1

very much on the same catalysts with three different supercell sizes. Then, we compare the adsorption energy of CO on three-layer model with those on four-layer and five-layer models, respectively, indicating that the corresponding adsorption energy are −87.0, −87.9 and −85.0 kJ/mol on the Pd_4Cu_8/Cu(111) surface, −101.2, −101.8 and −100.0 kJ/mol on the Pd_1-Cu(111) surface, which implies that there has little influence when the layer of model increases. Thus, taking account of the calculation efficiency, the selected p(3 × 4) supercell and three-layer model are also considered to be sufficient for the calculated systems.

And, we consider the influence of dipole correction on the binding energy between Pd stripe or Pd single atom with Cu(111) surface as well as the elementary reaction process. The results indicate that the binding energies with dipole correction are −1460.0 and −604.0 kJ/mol for Pd_4Cu_8/Cu(111) and Pd_1-Cu(111), respectively, and very close to the values of −1458.6 and −603.9 kJ/mol without dipole correction, where the binding energy is obtained by the energy of model subtracting the sum of doped Pd atom energy and defective Cu(111) energy according to previous work [90]. Meanwhile, the energy barrier and reaction energy of the first elementary step ($CO + OCH_3 \rightarrow COOCH_3$) are 25.4 and −40.6 (25.8 and −40.4) kJ/mol on Pd_4Cu_8/Cu(111), 55.4 and 24.0 (55.3 and 23.3) kJ/mol on Pd_1-Cu(111), which are very close to the values obtained without dipole correction (see the values in parentheses). That all show that little difference exists when the dipole correction is added into system. Therefore, dipole correction is neglected in this study. The previous study also adopted the same treatment method owing to little influence of the dipole correction [91,92].

3. Results and discussion

3.1. Catalytic activities of Pd_4Cu_8/Cu(111) and Pd_1-Cu(111) surfaces toward DMO formation

As is well known that CH_3ONO molecular is very easily dissociated to OCH_3 radical because of the weak O-NO bond energy [8–10], therefore it is OCH_3 radical that launches DMO generation. In light of different C—C coupling patterns, there exists three possible pathways for DMO formation, i.e. $COOCH_3$-$COOCH_3$ coupling (Path1), CO-$COOCH_3$ coupling (Path2) and CO-CO coupling (Path3). Among them, OCCO intermediate in Path3 is extremely unstable and easily dissociated into two CO on surfaces of Pd_4Cu_8/Cu(111) and Pd_1-Cu(111), therefore only Path1 and Path2 will be discussed in the following sections, as shown in Scheme 1. The activation energy and reaction energy of each elementary step, E_a and ΔE, which involved in DMO synthesis on surfaces of Pd_4Cu_8/Cu(111) and Pd_1-Cu(111), have been presented in Table 2.

3.1.1. Catalytic activity for DMO generation on the surface of Pd_4Cu_8/Cu(111)

The surface layer striped Pd atoms of Pd(111) and Pd_{ML}/Cu(111) have been found to be main active sites for DMO formation [12], therefore we mainly focus on investigating DMO synthesis over the Pd

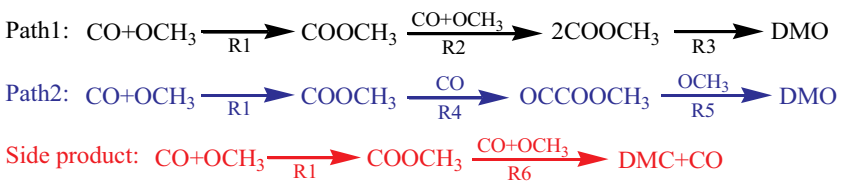

Scheme 1. Proposed routes [13] for DMO generation via CO oxidative coupling.

Table 2
The energy barrier and reaction heat for each elementary step (E_a and ΔE, kJ/mol) together with the rate constant (k, s^{-1}) at the temperature of 395 K.

Surface	Elementary reactions		Transition state	E_a	ΔE	k
Pd_4Cu_8/Cu(111)	R1	$CO + OCH_3 \rightarrow COOCH_3$	TS1	25.8	−40.4	1.01×10^{9}
	R2	$COOCH_3 + CO + OCH_3 \rightarrow 2COOCH_3$	TS2	88.3	52.0	9.95×10^{0}
	R3	$2COOCH_3 \rightarrow (COOCH_3)_2$	TS3	108.8	−30.6	2.70×10^{-2}
	R4	$COOCH_3 + CO \rightarrow OCCOOCH_3$	TS4	139.3	74.4	3.64×10^{-6}
	R5	$OCCOOCH_3 + OCH_3 \rightarrow (COOCH_3)_2$	TS5	34.1	−74.5	3.48×10^{7}
	R6	$COOCH_3 + CO + OCH_3 \rightarrow DMC + CO$	TS6	192.6	−52.7	4.79×10^{-13}
Pd_1-Cu(111)	R1	$CO + OCH_3 \rightarrow COOCH_3$	TS1	55.3	23.3	1.75×10^{5}
	R2	$COOCH_3 + CO + OCH_3 \rightarrow 2COOCH_3$	TS2	65.5	34.0	4.91×10^{3}
	R3	$2COOCH_3 \rightarrow (COOCH_3)_2$	TS3	91.6	−26.4	4.42×10^{1}
	R4	$COOCH_3 + CO \rightarrow OCCOOCH_3$	TS4	130.0	55.0	5.31×10^{-4}
	R5	$OCCOOCH_3 + OCH_3 \rightarrow (COOCH_3)_2$	TS5	58.8	−41.0	2.38×10^{4}
	R6	$COOCH_3 + CO + OCH_3 \rightarrow DMC + CO$	TS6	107.5	−27.7	5.45×10^{-3}
Pd_{ML}/Cu(111)[a]	R1	$CO + OCH_3 \rightarrow COOCH_3$	TS1	15.6	−87.5	6.07×10^{9}
	R2	$COOCH_3 + CO + OCH_3 \rightarrow 2COOCH_3$	TS2	45.6	−25.7	1.51×10^{6}
	R3	$2COOCH_3 \rightarrow (COOCH_3)_2$	TS3	132.2	−34.1	6.98×10^{-6}
	R4	$COOCH_3 + CO \rightarrow OCCOOCH_3$	TS4	151.5	84.3	1.01×10^{-7}
	R5	$OCCOOCH_3 + OCH_3 \rightarrow (COOCH_3)_2$	TS5	166.1	−130.2	2.00×10^{-8}
	R6	$COOCH_3 + CO + OCH_3 \rightarrow DMC + CO$	TS6	194.8	−172.4	5.10×10^{-13}
Pd(111)[a]	R1	$CO + OCH_3 \rightarrow COOCH_3$	TS1	38.1	−25.6	3.97×10^{6}
	R2	$COOCH_3 + CO + OCH_3 \rightarrow 2COOCH_3$	TS2	52.5	−17.5	5.87×10^{4}
	R3	$2COOCH_3 \rightarrow (COOCH_3)_2$	TS3	120.6	53.6	3.35×10^{-5}
	R4	$COOCH_3 + CO \rightarrow OCCOOCH_3$	TS4	160.1	117.0	2.12×10^{-9}
	R5	$OCCOOCH_3 + OCH_3 \rightarrow (COOCH_3)_2$	TS5	31.2	−43.2	6.81×10^{8}
	R6	$COOCH_3 + CO + OCH_3 \rightarrow DMC + CO$	TS6	153.5	−110.8	1.79×10^{-8}

[a] The study in Ref. [12].

stripe of the Pd_4Cu_8/Cu(111) surface. Firstly, Path1 is initiated by co-adsorption of CO and OCH_3, where OCH_3 and CO are adsorbed at Pd—Pd bridge and Pd top sites with co-adsorption energy being −224.1 kJ/mol, which is revealed in Fig. 2. Subsequently, OCH_3 oxidizes CO to generate a highly stable intermediate of $COOCH_3$ via TS1 with the energy barrier, reaction energy and rate constant being 25.8, −40.4 kJ/mol and $1.01 \times 10^{9}\ s^{-1}$, where C1···O2 distance decreases to 2.172 from 4.258 Å (All described rate constants are obtained at 395 K, as presented in Table 2. And the rate constants at other temperatures are shown in Table 3). The formed $COOCH_3$ occupies the Pd top site, as well as the other CO and OCH_3 bind to the Pd—Pd bridge and Pd-Cu-Cu hcp sites, respectively. Then the adsorbed OCH_3 and CO are activated via TS2 to generate the second $COOCH_3$ intermediate, thereby leading to $COOCH_3$-$COOCH_3$ formation, which is endergonic (52.0 kJ/mol) together with the activation energy being 88.3 kJ/mol. The C3···O4 distance in TS2 configuration is reduced to 1.997 from 3.411 Å. Finally, DMO can be formed by the $COOCH_3$-$COOCH_3$ intermediate self-coupling, which is exergonic (30.6 kJ/mol) with the activation energy and rate constant being 108.8 kJ/mol and $2.70 \times 10^{-2}\ s^{-1}$. The step is considered as the speed-controlling step in Path1, of which the activation barrier is lower to those (120.6 and 132.2 kJ/mol) while the rate constant is far bigger than those over Pd(111) and Pd_{ML}/Cu(111) (3.35×10^{-5} and $6.98 \times 10^{-6}\ s^{-1}$) [12]. Thus, it can be concluded that catalytic activity of Path1 on Pd_4Cu_8/Cu(111) is more than those on Pd(111) and Pd_{ML}/Cu(111).

In Path2, the formed $COOCH_3$ of first step is further activated to attack CO which locates at the Pd—Pd bridge site, leading to $OCCOOCH_3$ generation through TS4 with the activation energy, reaction heat and rate constant being 139.3, 74.4 kJ/mol and $3.64 \times 10^{-6}\ s^{-1}$. At last, OCH_3 occupies on the Pd-Cu-Cu hcp site and attacks $OCCOOCH_3$ to generate DMO via TS5 with the rate constant, activation energy and reaction heat being $3.48 \times 10^{7}\ s^{-1}$, 34.1 and −74.5 kJ/mol. It is found that the second step, $COOCH_3 + CO \rightarrow OCCOOCH_3$, is the rate-controlling step of Path 2, of which activation barrier is relatively higher in comparison with that of Path1 (139.3 versus 108.8 kJ/mol). Accordingly, Path1 is considered to be the optimal reaction path on the surface of Pd_4Cu_8/Cu(111), which determines the catalytic activity of DMO formation.

3.1.2. Catalytic activity of the Pd_1-Cu(111) surface for DMO generation

On basis of the research over Pd_4Cu_8/Cu(111), to further reduce the amount of precious metal Pd, we study CO oxidation to DMO over the Pd_1-Cu(111). $CO + OCH_3 \rightarrow COOCH_3$ is the first step of Path1, as depicted in Fig. 3, where OCH_3 and CO are bind to Cu—Cu and Pd—Cu bridge sites, afterwards $COOCH_3$ intermediate is generated through OCH_3 oxidizing CO via TS1 with the endothermic energy and activation energy being 23.3 and 55.3 kJ/mol. Additionally, the C1···O2 distance is shorten to 1.822 in TS1 from 3.553 Å. The other $COOCH_3$ can be formed through TS2, resulting in the $COOCH_3$-$COOCH_3$ intermediate formation, which is endothermic by 34.0 kJ/mol together with a barrier energy being 65.5 kJ/mol. Lastly, the $COOCH_3$-$COOCH_3$ intermediate self-couples to DMO via TS3, and the barrier energy of 91.6 kJ/mol, reaction energy being −26.4 kJ/mol and rate constant of $4.42 \times 10^{1}\ s^{-1}$ are needed in this step.

In Path2, the generated $COOCH_3$ can react with CO to produce $OCCOOCH_3$ by TS4 with C1···C3 distance being 2.010 Å, and the activation barrier, reaction energy and rate constant are 130.0, 55.0 kJ/mol and $5.31 \times 10^{-4}\ s^{-1}$. Then, OCH_3 and $OCCOOCH_3$ are activated to generate DMO through TS5 with the reaction energy being −41.0 kJ/mol, activation barrier being 58.8 kJ/mol and rate constant of $2.38 \times 10^{4}\ s^{-1}$. As described above, R3 and R4 are the rate-controlling steps of Path1 and Path2 over the Pd_1-Cu(111) with the barriers being 91.6 and 130.0 kJ/mol, respectively, implying the favorable pathway is Path1. In addition, comparing the barriers (132.2 [12], 108.8 and 91.6 kJ/mol) of the rate-controlling steps of the optimal path on surfaces of Pd_{ML}/Cu(111) [12], Pd_4Cu_8/Cu(111) and Pd_1-Cu(111), it is drawn that Pd_1-Cu(111) is better than Pd_{ML}/Cu(111) and Pd_4Cu_8/Cu(111) in terms of catalytic activity.

3.2. Comparison of DMO and DMC synthesis on Pd_4Cu_8/Cu(111) and Pd_1-Cu(111) surfaces

In addition to investigating the generation of the main product DMO, we also consider side-product dimethyl carbonate ($CH_3OCOOCH_3$, DMC) synthesis. DMC can be formed by the $COOCH_3$ reacting with OCH_3 on the basis of co-adsorption of $COOCH_3 + CO + OCH_3$, where the impact of CO on DMC formation is considered owing to excessive CO in the practical reaction [13]. On

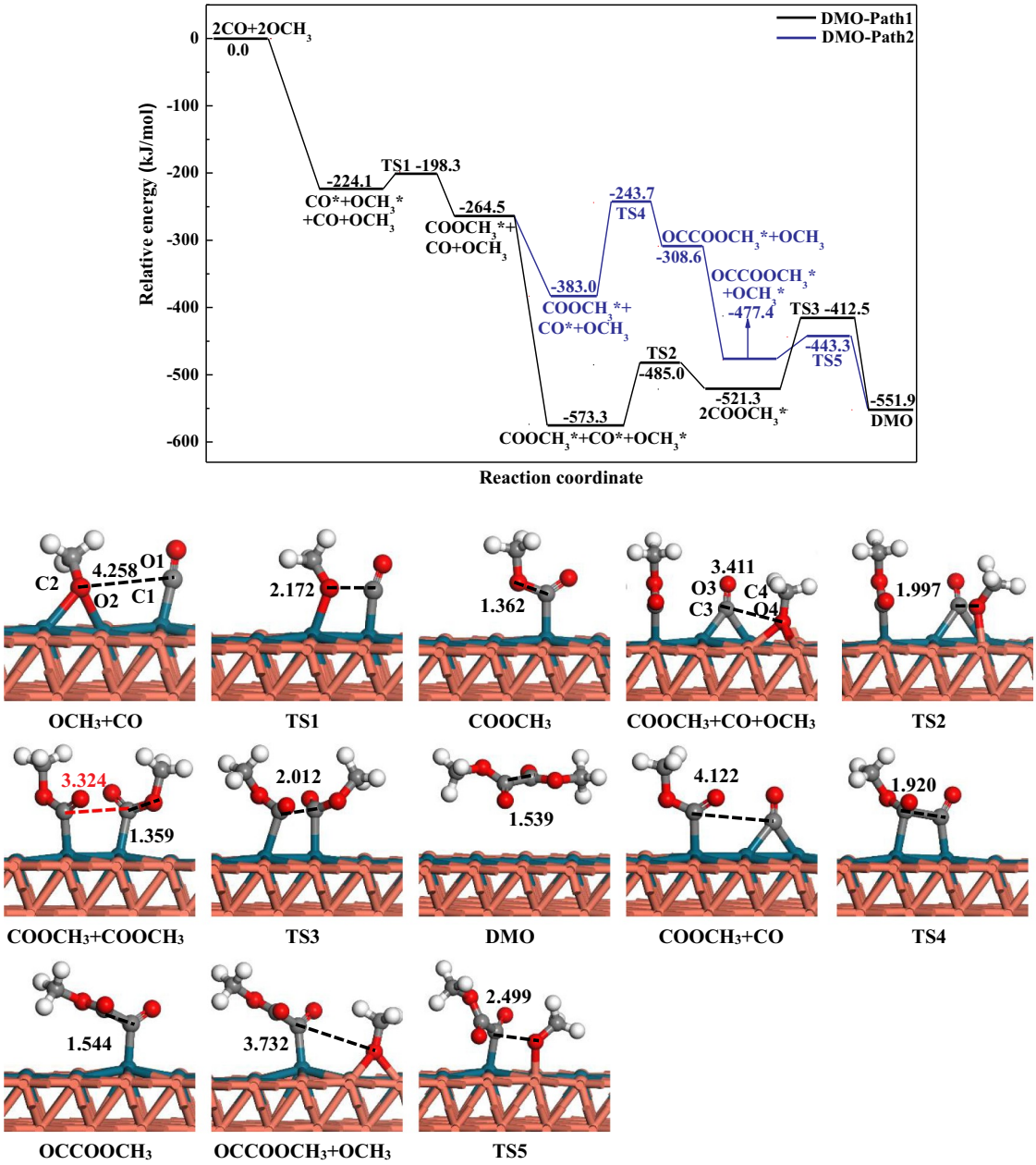

Fig. 2. Reaction energy profile of CO oxidation to DMO and relevant configurations (initial, transition and final states) over the Pd_4Cu_8/Cu(111).

Table 3
The rate constant (k, s^{-1}) of each elementary step.

		375 K	385 K	395 K	405 K	415 K
Pd_4Cu_8/Cu(111)	k_1	6.59×10^{8}	8.19×10^{8}	1.01×10^{9}	1.23×10^{9}	1.48×10^{9}
	k_2	2.31×10^{0}	4.89×10^{0}	9.95×10^{0}	1.96×10^{1}	3.72×10^{1}
	k_3	4.51×10^{-3}	1.13×10^{-2}	2.70×10^{-2}	6.19×10^{-2}	1.36×10^{-1}
	k_4	3.69×10^{-7}	1.19×10^{-6}	3.64×10^{-6}	1.05×10^{-5}	2.88×10^{-5}
	k_5	2.00×10^{7}	2.66×10^{7}	3.48×10^{7}	4.49×10^{7}	5.73×10^{7}
	k_6	1.98×10^{-14}	1.02×10^{-13}	4.79×10^{-13}	2.10×10^{-12}	8.54×10^{-12}
Pd_1-Cu(111)	k_1	7.05×10^{4}	1.12×10^{5}	1.75×10^{5}	2.66×10^{5}	3.97×10^{5}
	k_2	1.68×10^{3}	2.91×10^{3}	4.91×10^{3}	8.07×10^{3}	1.29×10^{4}
	k_3	9.64×10^{0}	2.11×10^{1}	4.42×10^{1}	8.95×10^{1}	1.75×10^{2}
	k_4	6.21×10^{-5}	1.87×10^{-4}	5.31×10^{-4}	1.43×10^{-3}	3.69×10^{-3}
	k_5	9.00×10^{3}	1.48×10^{4}	2.38×10^{4}	3.72×10^{4}	5.71×10^{4}
	k_6	9.57×10^{-4}	2.34×10^{-3}	5.45×10^{-3}	1.22×10^{-2}	2.62×10^{-2}

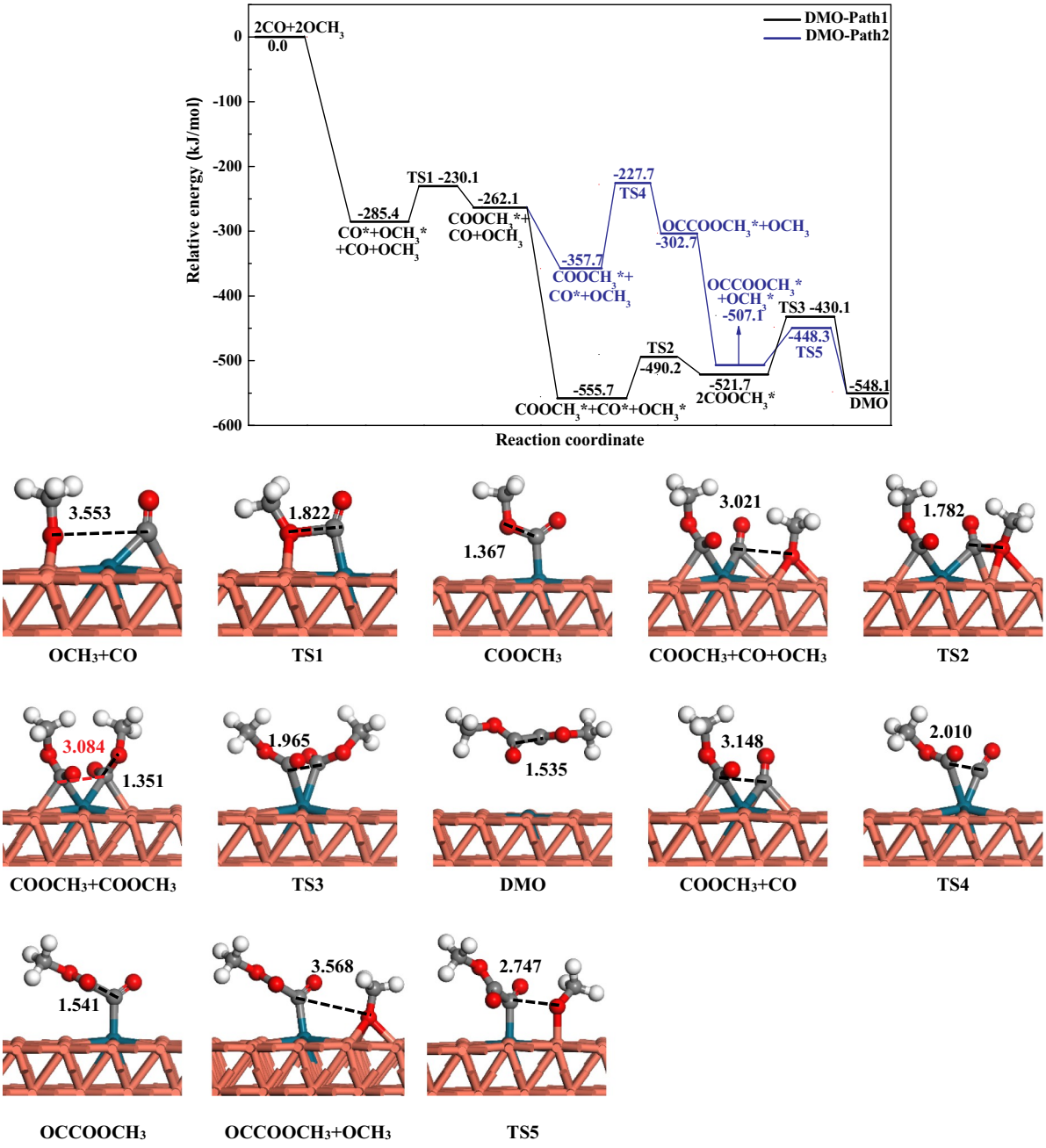

Fig. 3. Reaction energy profile of CO oxidation to DMO and relevant structures (initial, transition and final states) over the Pd_1-Cu(111).

Pd_4Cu_8/Cu(111), it can be drawn that DMC is not favorable to be formed by comparing the energy barriers (192.6 versus 108.8) of rate-determining step in favorable path of produced DMO and DMC, which is depicted in Fig. 4. Similarly, the activation barrier (107.5 kJ/mol) of DMC generation is more than that (91.6 kJ/mol) of $2COOCH_3 \rightarrow$ DMO in favorable route on the Pd_1-Cu(111) surface, showing that DMO formation is significantly superior to DMC generation, which is shown in Fig. 5. Therefore, the main product DMO is more easier to be generated than the side-product (DMC) over Pd_4Cu_8/Cu(111) and Pd_1-Cu(111).

3.3. Microkinetic analysis

On the basis of obtained activation energy of each elementary step, we can know that the optimal route for DMO formation is Path1 ($COOCH_3$-$COOCH_3$ coupling) and the rate-controlling step is two $COOCH_3$ intermediates coupling to DMO. According to activation energy for the speed-controlling step of optimal path for DMO generation, we can know that the catalytic activity is highest on the Pd_1-Cu (111) surface, and Pd_4Cu_8/Cu(111) is higher than Pd(111), as well as Pd_{ML}/Cu(111) exhibits the lowest activity, as revealed in Fig. 6.

In order to further understand CO oxidation to DMO over Pd_4Cu_8/Cu (111) and Pd_1-Cu(111) at the practical condition with temperatures (T: 375–415 K) and pressures (P_{CO}: 280 kPa, P_{CH3ONO}: 200 kPa) [19], the microkinetic model [11,12,93–96] on the basis of transition state theory is implemented in the present study. Firstly, adsorption equilibrium constants (K) of initial reactants (OCH_3 and CO) are acquired by the formulas (5)–(6) when it is assumed that the adsorption processes are in equilibrium. Secondly, the coverage of OCH_3, CO, $COOCH_3$ and $OCCOOCH_3$ are obtained by the formulas (7)–(11). Lastly, the generation rates of DMO and DMC can be obtained the formulas: $r_{DMO} = k_3\theta_{COOCH_3}{}^2 + k_5\theta_{OCCOOCH_3}\theta_{OCH_3}$ (12) and $r_{DMC} = k_6\theta_{COOCH_3}\theta_{OCH_3}$ (13), respectively. The calculated adsorption equilibrium constants, coverages and formation rates are presented in Table 4,

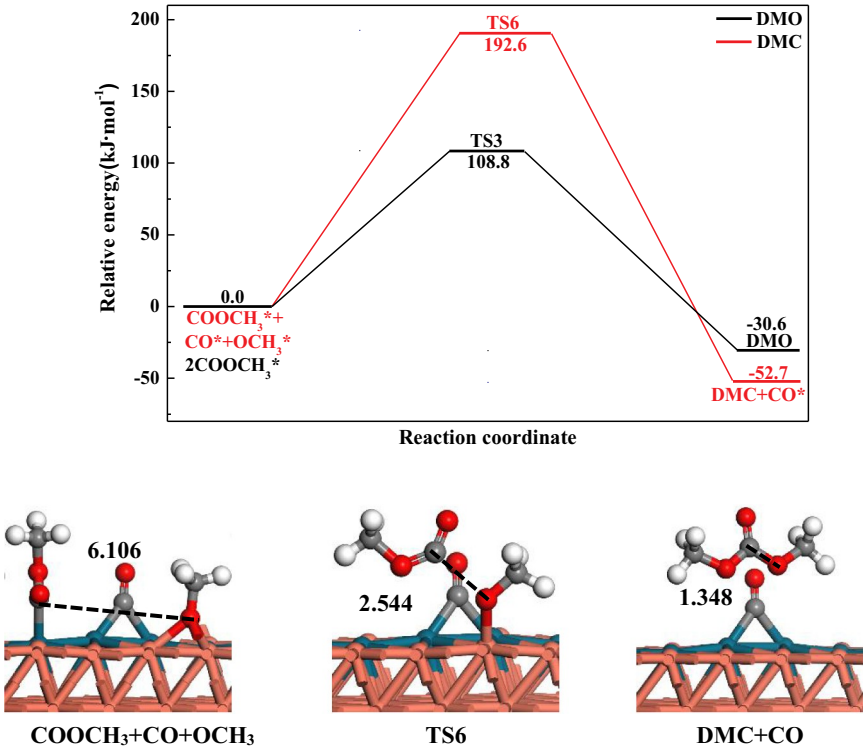

Fig. 4. The comparison of the potential energy profile for the rate-determining step in favorable reaction path toward DMO and DMC synthesis over the Pd_4Cu_8/Cu (111) surface.

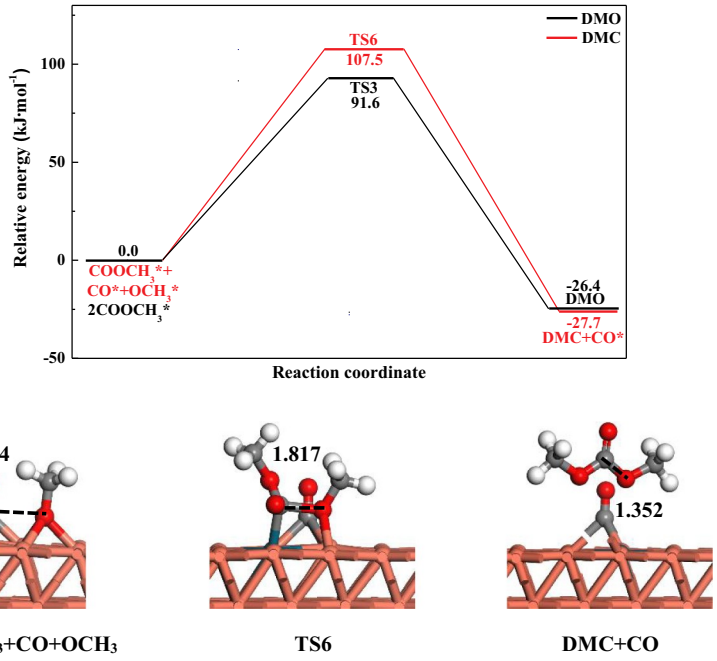

Fig. 5. The comparison of the potential energy profile for the rate-determining step in favorable reaction path toward DMO and DMC synthesis over the Pd_1-Cu(111) surface.

Table 5, and Table 6, respectively.

$$K = \exp[-(\Delta E_{ads} - T(S_{adsorbate} - S_{gas}))/RT] \quad (5)$$

$$S = R\sum_{i=1}^{3N}\left[-\ln\left(1-\exp\left(-\frac{h\nu_i}{k_B T}\right)\right) + \frac{h\nu_i}{k_B T}\frac{\exp\left(-\frac{h\nu_i}{k_B T}\right)}{1-\exp\left(-\frac{h\nu_i}{k_B T}\right)}\right] \quad (6)$$

where ΔE_{ads} refers to the adsorption energies of OCH_3 or CO. $S_{adsorbate}$ represents entropies of the adsorbed OCH_3 and CO over Pd_4Cu_8/Cu(111) and Pd_1-Cu(111) surfaces. S_{gas} represents gas phase entropy, which can be obtained by the Eq. (6) [97].

$$\theta_{CO} = P_{CO}K_{CO}\theta^* \quad (7)$$

$$\theta_{OCH_3} = P_{OCH_3}K_{OCH_3}\theta^* \quad (8)$$

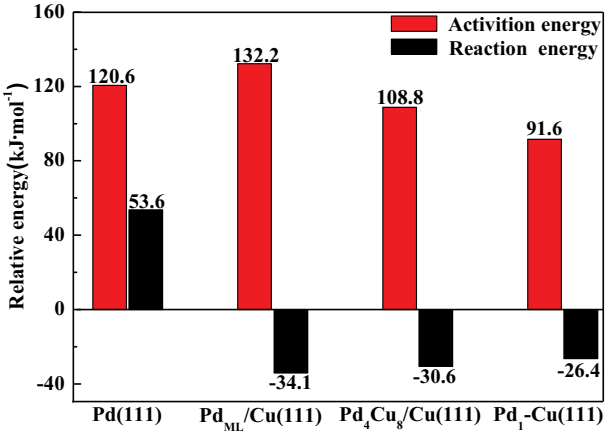

Fig. 6. The reaction energy profile for the speed-determining step ($2COOCH_3 \rightarrow DMO$) in optimal path for DMO generation on surfaces of Pd (111), Pd_{ML}/Cu(111), Pd_4Cu_8/Cu(111) and Pd_1-Cu(111).

$$\theta_{COOCH_3}: \frac{d\theta_{COOCH_3}}{dt} = k_1\theta_{OCH_3}\theta_{CO} + k_2\theta_{OCH_3}\theta_{CO} - k_3\theta^2_{COOCH_3} - k_4\theta_{COOCH_3}\theta_{CO} - k_6\theta_{COOCH_3}\theta_{OCH_3} = 0 \quad (9)$$

$$\theta_{OCCOOCH_3}: \frac{d\theta_{OCCOOCH_3}}{dt} = k_4\theta_{COOCH_3}\theta_{CO} - k_5\theta_{OCCOOCH_3}\theta_{OCH_3} = 0 \quad (10)$$

$$\theta_{CO} + \theta_{OCH_3} + \theta_{COOCH_3} + \theta_{OCCOOCH_3} + \theta^* = 1 \quad (11)$$

As revealed in Table 6, the order of DMO formation rate is Pd_1-Cu (111) > Pd_4Cu_8/Cu(111) > Pd(111) > Pd_{ML}/Cu(111) and the rate of DMO generation is found to be far higher than that of DMC formation over Pd_4Cu_8/Cu(111) and Pd_1-Cu(111), which agrees well with the analysis via activation barrier as well as rate constants. As a consequence, Pd_4Cu_8/Cu(111) and Pd_1-Cu(111) surfaces exhibit remarkable activity and selectivity for DMO formation. The same microkinetic analysis has been adopted to acquire that activity for DMO synthesis on the Pd_{ML}/Cu(111) was weaker than that on the Pd(111) [12].

3.4. Strain versus ligand effect on catalytic activity for DMO synthesis

As mentioned above, the catalytic activity for DMO synthesis is Pd_1-Cu(111) > Pd_4Cu_8/Cu(111) > Pd_{ML}/Cu(111), which increases as the amount of Pd decreases. In bimetallic catalysts system, the strain and ligand effect together affect the catalytic activity, where the strain effect occurs when the bond length of surface metal-metal is compressed or expanded by the substrate metal and the ligand effect arises when electrons transfer between two different metal atoms [66–75]. The calculated average bond length between Pd and surrounding atoms on surfaces of Pd(111), Pd_{ML}/Cu(111), Pd_4Cu_8/Cu(111) and Pd_1-Cu(111) are 2.797, 2.650 [12], 2.577 and 2.601 Å, respectively, indicating that Cu substrates cause the contraction of average bond length between Pd and surrounding atoms, which is termed the strain effect, as well as the values of contraction strain (ξ) are −5.3%, −7.9% and −7.0%, respectively. Average charge polarization (Δσ) of surface Pd atoms over Pd_{ML}/Cu(111), Pd_4Cu_8/Cu(111) and Pd_1-Cu(111) are obtained by the Bader charge and the values are −0.14 [12], −0.28, and − 0.37 e, respectively, indicating that the charge transfer to surface Pd from Cu substrates, which is known as the ligand effect. It can be thought that different contents of Pd atoms cause different strain and ligand effects, thereby resulting in different catalytic activity. Nevertheless, the co-existence of the strain and ligand effect conceals underlying origin of the changed activity of bimetallic catalysts. Thence, it is essential to decouple strain and ligand effect so as to comprehend individual impact on activity.

Taking account of calculation efficiency, the speed-controlling step ($2COOCH_3 \rightarrow DMO$) that determines the catalytic activity is chosen to investigate how the strain and ligand effect influence the activity of Pd_4Cu_8/Cu(111) and Pd_1-Cu(111). According to previous work [68,71,98], the strain contribution (ΔE_a^{strain}), the ligand contribution (ΔE_a^{ligand}) and combined contribution ($\Delta E_a^{combined}$) can be calculated via Eqs. (14)–(16), where $E_a^{Strain\text{-}M}$ stands for the activation barrier on strained monometallic Pd(111) surface, E_a^{Pd} refers to the activation barrier on the Pd(111) surface, $E_a^{Pd\text{-}M}$ represents the activation barrier on Pd_4Cu_8/Cu(111) or Pd_1-Cu(111) surfaces. For instance, on the Pd_4Cu_8/Cu(111), based on the calculated $E_a^{Strain\text{-}M}$, E_a^{Pd} and $E_a^{Pd\text{-}M}$ (172.5, 120.6 and 108.8 kJ/mol) combined with Eqs. (14)–(16), ΔE_a^{strain}, ΔE_a^{ligand} and $\Delta E_a^{combined}$ can be obtained and the values are 51.9, −63.7 and − 11.8 kJ/mol, respectively.

$$\Delta E_a^{strain} = E_a^{strain\text{-}M} - E_a^{Pd} \quad (14)$$

$$\Delta E_a^{ligand} = E_a^{Pd\text{-}M} - E_a^{strain\text{-}M} \quad (15)$$

$$\Delta E_a^{combined} = \Delta E_a^{strain} + \Delta E_a^{ligand} \quad (16)$$

In the case of Pd_4Cu_8/Cu(111) surface, the strain effect enlarges the activation energy while ligand effect is opposite, where the ligand effect is dominant factor, therefore its catalytic is enhanced, as revealed in Fig. 7. On the surface of Pd_1-Cu(111), strain effect has a decrease on activation barrier while ligand effect has an increase on it, and strain effect prevails to ligand effect, leading to the catalytic activity increased, which is similar to the case over Pd_{ML}/Co(111) and Pd_{ML}/Ni (111) [11]. This method has been also successfully employed in explaining that the relatively low activity for DMO generation on the Pd_{ML}/Cu(111) was because weak strain effect reduced activation barrier while strong ligand effect enlarged it [12].

4. Conclusions

Density functional theory (DFT) and microkinetic model have been employed in studying CO oxidation to DMO over Pd_4Cu_8/Cu(111) and Pd_1-Cu(111) surfaces to search low Pd usage of Pd—Cu bimetallic catalysts in the presupposition of keeping its catalytic performance. It has been obtained that the optimal pathway is $CO + CH_3O \rightarrow COOCH_3 + (CO + OCH_3) \rightarrow 2COOCH_3 \rightarrow DMO$ over these two catalysts, in which the rate-determining step is $2COOCH_3 \rightarrow DMO$. The analysis result of energy barrier in conjunction with microkinetic model indicates that the activity for DMO formation is in sequence of Pd_1-Cu (111) > Pd_4Cu_8/Cu(111) > Pd(111) > Pd_{ML}/Cu(111). The outstanding activity of Pd_4Cu_8/Cu(111) for DMO formation are ascribed to weak strain effect and strong ligand effect, where strain effect increases activation barrier while ligand effect reduces it. The opposite of this arises over the Pd_1-Cu(111) surface. In addition, DMO formation is favorable than synthesis of side-product (DMC) on surfaces of Pd_4Cu_8/

Table 4
The reaction equilibrium constants of CO and OCH_3.

		375 K	385 K	395 K	405 K	415 K
Pd_4Cu_8/Cu(111)	K_{CO}	2.60×10^7	1.25×10^7	6.23×10^6	3.21×10^6	1.71×10^6
	K_{OCH3}	1.48×10^{16}	4.63×10^{15}	1.53×10^{15}	5.36×10^{14}	1.97×10^{14}
Pd_1-Cu(111)	K_{CO}	1.65×10^9	7.06×10^8	3.14×10^8	1.46×10^8	7.02×10^7
	K_{OCH3}	1.30×10^{14}	7.46×10^{13}	2.82×10^{13}	1.12×10^{13}	4.63×10^{12}

Table 5
The surface coverage for different species.

		375 K	385 K	395 K	405 K	415 K
Pd_4Cu_8/Cu(111)	θ^*	1.69×10^{-23}	6.16×10^{-23}	2.10×10^{-22}	6.71×10^{-22}	2.03×10^{-21}
	θ_{CO}	1.23×10^{-10}	2.15×10^{-10}	3.65×10^{-10}	6.04×10^{-10}	9.73×10^{-10}
	θ_{OCH3}	5.01×10^{-2}	5.70×10^{-2}	6.43×10^{-2}	7.20×10^{-2}	8.01×10^{-2}
	θ_{COOCH3}	9.50×10^{-1}	9.43×10^{-1}	9.36×10^{-1}	9.28×10^{-1}	9.20×10^{-1}
	$\theta_{OCCOOCH3}$	4.31×10^{-23}	1.60×10^{-22}	5.57×10^{-22}	1.82×10^{-21}	5.62×10^{-21}
Pd_1-Cu(111)	θ^*	2.81×10^{-20}	5.28×10^{-20}	1.42×10^{-19}	3.62×10^{-19}	8.83×10^{-19}
	θ_{CO}	1.30×10^{-5}	1.04×10^{-5}	1.25×10^{-5}	1.48×10^{-5}	1.74×10^{-5}
	θ_{OCH3}	7.33×10^{-1}	7.88×10^{-1}	7.99×10^{-1}	8.09×10^{-1}	8.18×10^{-1}
	θ_{COOCH3}	2.67×10^{-1}	2.12×10^{-1}	2.01×10^{-1}	1.91×10^{-1}	1.82×10^{-1}
	$\theta_{OCCOOCH3}$	3.27×10^{-14}	3.54×10^{-14}	7.03×10^{-14}	1.35×10^{-13}	2.50×10^{-13}

Table 6
The generation rates (s^{-1}·site^{-1}) for DMO and DMC.

		375 K	385 K	395 K	405 K	415 K
Pd_4Cu_8/Cu(111)	DMO	4.07×10^{-3}	1.00×10^{-2}	2.36×10^{-2}	5.33×10^{-2}	1.15×10^{-1}
	DMC	9.43×10^{-16}	5.46×10^{-15}	2.88×10^{-14}	1.40×10^{-13}	6.30×10^{-13}
Pd_1-Cu(111)	DMO	6.88×10^{-1}	9.47×10^{-1}	1.79×10^{0}	3.27×10^{0}	5.81×10^{0}
	DMC	1.87×10^{-4}	3.90×10^{-4}	8.76×10^{-4}	1.89×10^{-3}	3.91×10^{-3}
Pd(111)[a]	DMO	4.72×10^{-6}	1.29×10^{-5}	3.35×10^{-5}	5.31×10^{-5}	1.98×10^{-4}
	DMC	4.02×10^{-14}	2.45×10^{-13}	1.11×10^{-12}	4.02×10^{-12}	6.04×10^{-12}
Pd_{ML}/Cu(111)[a]	DMO	7.92×10^{-7}	2.42×10^{-6}	6.98×10^{-6}	1.91×10^{-5}	2.71×10^{-5}
	DMC	5.67×10^{-20}	4.44×10^{-19}	3.14×10^{-18}	2.01×10^{-17}	2.96×10^{-17}

[a] The study in Ref [12].

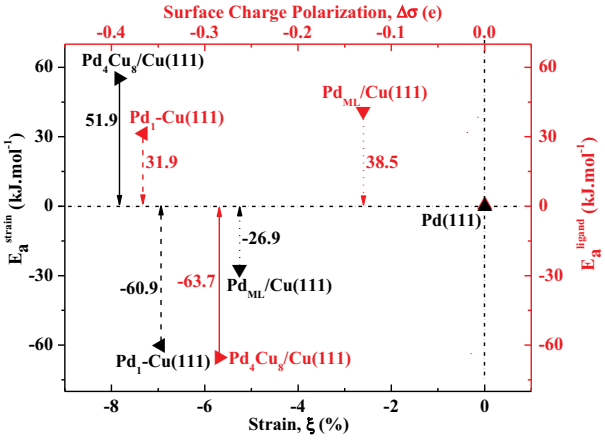

Fig. 7. The comparison of strain contribution and ligand contribution for $2COOCH_3 \rightarrow DMO$.

Cu(111) and Pd_1-Cu(111). Hence, we suggest that the Pd_4Cu_8/Cu(111) and Pd_1-Cu(111) can be attempted in experiment to improve the performance of catalytic DMO formation and cut down the cost.

Acknowledgments

We gratefully acknowledge financial support from the Key Projects of National Natural Science Foundation of China (21736007), the National Natural Science Foundation of China (Grant Nos. 21576178 and 21476155), Research Project Supported by Shanxi Scholarship Council of China (No. 2016-030) and the Foundation of State Key Laboratory of Coal Conversion (No. J18-19-602).

References

[1] Y.J. Zhao, S.M. Li, Y. Wang, B. Shan, J. Zhang, S.P. Wang, X.B. Ma, Efficient tuning of surface copper species of Cu/SiO_2 catalyst for hydrogenation of dimethyl oxalate to ethylene glycol, Chem. Eng. J. 313 (2017) 759–768.
[2] H.R. Yue, Y.J. Zhao, L. Zhao, J. Lv, S.P. Wang, J.L. Gong, X.B. Ma, Hydrogenation of dimethyl oxalate to ethylene glycol on a Cu/SiO_2/cordierite monolithic catalyst: enhanced internal mass transfer and stability, AICHE J. 58 (2012) 2798–2809.
[3] A.Y. Yin, C. Wen, X.Y. Guo, W.L. Dai, K.N. Fan, Influence of Ni species on the structural evolution of Cu/SiO_2 catalyst for the chemoselective hydrogenation of dimethyl oxalate, J. Catal. 280 (2011) 77–88.
[4] A.Y. Yin, X.Y. Guo, W.L. Dai, K.N. Fan, The nature of active copper species in Cu-HMS catalyst for hydrogenation of dimethyl oxalate to ethylene glycol: new insights on the synergetic effect between Cu^0 and Cu^+, J. Phys. Chem. C 113 (2009) 11003–11013.
[5] A.Y. Yin, X.Y. Guo, W.L. Dai, H.X. Li, K.N. Fan, Highly active and selective copper-containing HMS catalyst in the hydrogenation of dimethyl oxalate to ethylene glycol, Appl. Catal. A Gen. 349 (2008) 91–99.
[6] Y.F. Zhu, Y.L. Zhu, G.Q. Ding, S.H. Zhu, H.Y. Zheng, Y.W. Li, Highly selective synthesis of ethylene glycol and ethanol via hydrogenation of dimethyl oxalate on Cu catalysts: influence of support, Appl. Catal. A Gen. 468 (2013) 296–304.
[7] D.M. Fenton, P.J. Steinwand, Noble metal catalysis. III. Preparation of dialkyl oxalates by oxidative carbonylation, J. Org. Chem. 39 (1974) 701–704.
[8] A.M. Wodtke, E.J. Hintsa, Y.T. Lee, The observation of CH_3O in the collision free multiphoton dissociation of CH_3NO_2, J. Chem. Phys. 84 (1986) 1044–1045.
[9] Z. Homayoon, J.M. Bowman, Quasiclassical trajectory study of CH_3NO_2 decomposition via roaming mediated isomerization using a global potential energy surface, J. Phys. Chem. A 117 (2013) 11665–11672.
[10] C. Fan, M. Luo, W.D. Xiao, Reaction mechanism of methyl nitrite dissociation during CO catalytic coupling to dimethyl oxalate: a density functional theory study, Chin. J. Chem. Eng. 24 (2016) 132–139.
[11] B.Y. Han, H. Lin, L.X. Ling, P. Liu, M.H. Fan, B.J. Wang, R.G. Zhang, A DFT study on dimethyl oxalate synthesis over Pd_{ML}/Ni(111) and Pd_{ML}/Co(111) surfaces, Appl. Surf. Sci. 465 (2019) 498–508.
[12] B.Y. Han, X. Feng, L.X. Ling, M.H. Fan, P. Liu, R.G. Zhang, B.J. Wang, CO oxidative coupling to dimethyl oxalate over Pd-Me (Me = Cu, Al) catalysts: a combined DFT and kinetic study, Phys. Chem. Chem. Phys. 20 (2018) 7317–7332.
[13] Q.H. Li, Z.F. Zhou, R.P. Chen, B.Z. Sun, L.Y. Qiao, Y.G. Yao, K.C. Wu, Insights into the reaction mechanism of CO oxidative coupling to dimethyl oxalate over palladium: a combined DFT and IR study, Phys. Chem. Chem. Phys. 17 (2015) 9126–9134.
[14] C.Z. Wang, P.J. Chen, Y.K. Li, G.F. Zhao, Y. Liu, Y. Lu, In situ DRIFTS study of CO coupling to dimethyl oxalate over structured Al-fiber@ns-AlOOH@Pd catalyst, J. Catal. 344 (2016) 173–183.
[15] F.D. Meng, G.H. Xu, R.Q. Guo, H.F. Yan, M.Q. Chen, Kinetic study of carbon monoxide coupling reaction over supported palladium catalyst, Chem. Eng. Process. 43 (2004) 785–790.
[16] C.Z. Wang, L.P. Han, P.J. Chen, G.F. Zhao, Y. Liu, Y. Lu, High-performance, low Pd-loading microfibrous-structured Al-fiber@ns-AlOOH@Pd catalyst for CO coupling to dimethyl oxalate, J. Catal. 337 (2016) 145–156.
[17] T.J. Zhao, D. Chen, Y.C. Dai, W.K. Yuan, A. Holmen, Synthesis of dimethyl oxalate from CO and CH_3ONO on carbon nanofiber supported palladium catalysts, Ind. Eng. Chem. Res. 43 (2004) 4595–4601.
[18] E.L. Jin, L.L. He, Y.L. Zhang, A.R. Richard, M.H. Fan, A nanostructured CeO_2 promoted Pd/a-alumina diethyl oxalate catalyst with high activity and stability, RSC Adv. 4 (2014) 48901–48904.

[19] Z.N. Xu, J. Sun, C.S. Lin, X.M. Jiang, Q.S. Chen, S.Y. Peng, M.S. Wang, G.C. Guo, High-performance and long-lived Pd nanocatalyst directed by shape effect for CO oxidative coupling to dimethyl oxalate, ACS Catal. 3 (2013) 118–122.

[20] S.Y. Peng, Z.N. Xu, Q.S. Chen, Z.Q. Wang, Y.M. Chen, D.M. Lv, G. Lu, G.C. Guo, MgO: an excellent catalyst support for CO oxidative coupling to dimethyl oxalate, Catal. Sci. Technol. 4 (2014) 1925–1930.

[21] S.Y. Peng, Z.N. Xu, Q.S. Chen, Y.M. Chen, J. Sun, Z.Q. Wang, M.S. Wang, G.C. Guo, An ultra-low Pd loading nanocatalyst with high activity and stability for CO oxidative coupling to dimethyl oxalate, Chem. Commun. 49 (2013) 5718–5720.

[22] X.G. Wang, G.S. Ma, F.C. Zhu, N.M. Lin, B. Tang, Z.H. Zhang, Preparation and characterization of micro-arc-induced Pd/TM(TM = Ni, Co and Ti) catalysts and comparison of their electrocatalytic activities toward ethanol oxidation, Electrochim. Acta 114 (2013) 500–508.

[23] J.M. Li, J.Y. Liu, Y. Yang, D. Qin, Bifunctional Ag@Pd-Ag nanocubes for highly sensitive monitoring of catalytic reactions by surface-enhanced raman spectroscopy, J. Am. Chem. Soc. 137 (2015) 7039–7042.

[24] Y.P. Li, S.M. Chen, R. Long, H.X. Ju, Z.W. Wang, X.X. Yu, F.Y. Gao, Z.J. Cai, C.M. Wang, Q. Xu, J. Jiang, J.F. Zhu, L. Song, Y.J. Xiong, Near-surface dilution of trace Pd atoms to facilitate Pd-H bond cleavage for giant enhancement of electrocatalytic hydrogen evolution, Nano Energy 34 (2017) 306–312.

[25] A. Groß, Reactivity of bimetallic systems studied from first principles, Top. Catal. 37 (2006) 29–39.

[26] R.G. Zhang, B. Zhao, L.L. He, A.J. Wang, B.J. Wang, Cost-effective promoter-doped Cu-based bimetallic catalysts for the selective hydrogenation of C_2H_2 to C_2H_4: the effect of the promoter on selectivity and activity, Phys. Chem. Chem. Phys. 20 (2018) 17487–17496.

[27] Z.L. Chen, J.F. Zhang, Y. Zhang, Y.W. Liu, X.P. Han, C. Zhong, W.B. Hu, Y.D. Deng, NiO-induced synthesis of PdNi bimetallic hollow nanocrystals with enhanced electrocatalytic activities toward ethanol and formic acid oxidation, Nano Energy 42 (2017) 353–362.

[28] Q.F. Zhang, X.P. Wu, G.F. Zhao, Y.K. Li, C.Z. Wang, Y. Liu, X.Q. Gong, Y. Lu, High-performance PdNi alloy structured in situ on monolithic metal foam for coalbed methane deoxygenation via catalytic combustion, Chem. Commun. 51 (2015) 12613–12616.

[29] Q.F. Zhang, Y.K. Li, R.J. Chai, G.F. Zhao, Y. Liu, Y. Lu, Low-temperature active, oscillation-free PdNi(alloy)/Ni-foam catalyst with enhanced heat transfer for coalbed methane deoxygenation via catalytic combustion, Appl. Catal. B Environ. 187 (2016) 238–248.

[30] Q.F. Zhang, X.P. Wu, Y.K. Li, R.J. Chai, G.F. Zhao, C.Z. Wang, X.Q. Gong, Y. Liu, Y. Lu, High-performance PdNi nanoalloy catalyst in situ structured on Ni foam for catalytic deoxygenation of coalbed methane: experimental and DFT studies, ACS Catal. 6 (2016) 6236–6245.

[31] Y.H. Zhao, S.G. Li, Y.H. Sun, Theoretical study on the dissociative adsorption of CH_4 on Pd-doped Ni surfaces, Chin. J. Catal. 34 (2013) 911–922.

[32] J.D. Cai, Y.Z. Zeng, Y.L. Guo, Copper@palladium-copper core-shell nanospheres as a highly effective electrocatalyst for ethanol electro-oxidation in alkaline media, J. Power Sources 270 (2014) 257–261.

[33] D.F. Wu, H.X. Xu, D.P. Cao, A. Fisher, Y. Gao, D.J. Cheng, PdCu alloy nanoparticle-decorated copper nanotubes as enhanced electrocatalysts: DFT prediction validated by experiment, Nanotechnology 27 (2016) 495403-1-11.

[34] Q. Fu, Y. Luo, Active sites of Pd-doped flat and stepped Cu(111) surfaces for H_2 dissociation in heterogeneous catalytic hydrogenation, ACS Catal. 3 (2013) 1245–1252.

[35] L.L. Ma, C.Q. Lv, G.C. Wang, A DFT study and micro-kinetic analysis of acetylene selective hydrogenation on Pd-doped Cu(111) surfaces, Appl. Surf. Sci. 410 (2017) 154–165.

[36] A.E. Baber, H.L. Tierney, T.J. Lawton, E.H. Sykes, An atomic-scale view of palladium alloys and their ability to dissociate molecular hydrogen, ChemCatChem 3 (2011) 607–614.

[37] X.R. Cao, Q. Fu, Y. Luo, Catalytic activity of Pd-doped Cu nanoparticles for hydrogenation as a single-atom-alloy catalyst, Phys. Chem. Chem. Phys. 16 (2014) 8367–8375.

[38] Q. Fu, Y. Luo, Catalytic activity of single transition-metal atom doped in Cu(111) surface for heterogeneous hydrogenation, J. Phys. Chem. C 117 (2013) 14618–14624.

[39] M.D. Marcinkowski, A.D. Jewell, M. Stamatakis, M.B. Boucher, E.A. Lewis, C.J. Murphy, G. Kyriakou, E.C.H. Sykes, Controlling a spillover pathway with the molecular cork effect, Nat. Mater. 12 (2013) 523–528.

[40] X.R. Cao, Y.F. Ji, Y. Luo, Dehydrogenation of propane to propylene by a Pd/Cu single-atom catalyst: insight from first-principles calculations, J. Phys. Chem. C 119 (2015) 1016–1023.

[41] M.T. Darby, R. Réocreux, E.C.H. Sykes, A. Michaelides, M. Stamatakis, Elucidating the stability and reactivity of surface intermediates on single-atom alloy catalysts, ACS Catal. 8 (2018) 5038–5050.

[42] M. Ramos, A.E. Martinez, H.F. Busnengo, H_2 dissociation on individual Pd atoms deposited on Cu(111), Phys. Chem. Chem. Phys. 14 (2012) 303–310.

[43] H.L. Tierney, A.E. Baber, J.R. Kitchin, E.C.H. Sykes, Hydrogen dissociation and spillover on individual isolated palladium atoms, Phys. Rev. Lett. 103 (2009) 246102-1-4.

[44] X.R. Cao, Insight into mechanism and selectivity of propane dehydrogenation over the Pd-doped Cu(111) surface, RSC Adv. 6 (2016) 65524–65532.

[45] X.X. Cao, A. Mirjalili, J. Wheeler, W.T. Xie, B.W.L. Jang, Investigation of the preparation methodologies of Pd-Cu single atom alloy catalysts for selective hydrogenation of acetylene, Front. Chem. Sci. Eng. 9 (2015) 442–449.

[46] C.M. Kruppe, J.D. Krooswyk, M. Trenary, Polarization-dependent infrared spectroscopy of adsorbed carbon monoxide to probe the surface of a Pd/Cu(111) single-atom alloy, J. Phys. Chem. C 121 (2017) 9361–9369.

[47] C.M. Kruppe, J.D. Krooswyk, M. Trenary, Selective hydrogenation of acetylene to ethylene in the presence of a carbonaceous surface layer on a Pd/Cu(111) single-atom alloy, ACS Catal. 7 (2017) 8042–8049.

[48] K.R. Yang, B. Yang, Surface restructuring of Cu-based single-atom alloy catalysts under reaction conditions: the essential role of adsorbates, Phys. Chem. Chem. Phys. 19 (2017) 18010–18017.

[49] Y.X. Yang, M.G. White, P. Liu, Theoretical study of methanol synthesis from CO_2 hydrogenation on metal-doped Cu(111) surfaces, J. Phys. Chem. C 116 (2012) 248–256.

[50] G. Kyriakou, M.B. Boucher, A.D. Jewell, E.A. Lewis, T.J. Lawton, A.E. Baber, H.L. Tierney, M. Flytzani-Stephanopoulos, E.C.H. Sykes, Isolated metal atom geometries as a strategy for selective heterogeneous hydrogenations, Science 335 (2012) 1209–1212.

[51] M.B. Boucher, B. Zugic, G. Cladaras, J. Kammert, M.D. Marcinkowski, T.J. Lawton, E.C.H. Sykes, M. Flytzani-Stephanopoulos, Single atom alloy surface analogs in $Pd_{0.18}Cu_{15}$ nanoparticles for selective hydrogenation reactions, Phys. Chem. Chem. Phys. 15 (2013) 12187–12196.

[52] G.X. Pei, X.Y. Liu, X.F. Yang, L.L. Zhang, A.Q. Wang, L. Li, H. Wang, X.D. Wang, T. Zhang, Performance of Cu-alloyed Pd single-atom catalyst for semihydrogenation of acetylene under simulated front-end conditions, ACS Catal. 7 (2017) 1491–1500.

[53] F. Studt, F. Abild-Pedersen, Q.X. Wu, A.D. Jensen, B. Temel, J.D. Grunwaldt, J.K. Nørskov, CO hydrogenation to methanol on Cu-Ni catalysts: theory and experiment, J. Catal. 293 (2012) 51–60.

[54] R.Y. Brogaard, R. Henry, Y. Schuurman, A.J. Medford, P.G. Moses, P. Beato, S. Svelle, J.K. Nørskov, U. Olsbye, Methanol-to-hydrocarbons conversion: the alkene methylation pathway, J. Catal. 314 (2014) 159–169.

[55] A.J. Medford, A.C. Lausche, F. Abild-Pedersen, B. Temel, N.C. Schjødt, J.K. Nørskov, F. Studt, Activity and selectivity trends in synthesis gas conversion to higher alcohols, Top. Catal. 57 (2014) 135–142.

[56] S. Dahl, A. Logadottir, C.J.H. Jacobsen, J.K. Nørskov, Electronic factors in catalysis: the volcano curve and the effect of promotion in catalytic ammonia synthesis, Appl. Catal. A Gen. 222 (2001) 19–29.

[57] N. Balakrishnan, B. Joseph, V.R. Bhethanabotla, Effect of platinum promoters on the removal of O from the surface of cobalt catalysts: a DFT study, Sur. Sci. 606 (2012) 634–643.

[58] T.L. Wind, H. Falsig, J. Sehested, P.G. Moses, T.T.M. Nguyen, Comparison of mechanistic understanding and experiments for CO methanation over nickel, J. Catal. 342 (2016) 105–116.

[59] K.Z. Qi, J.M. Zhao, G.C. Wang, A density functional theory study of ethylene hydrogenation on MgO- and γ-Al_2O_3-supported carbon-containing Ir_4 clusters, Phys. Chem. Chem. Phys. 17 (2015) 4899–4908.

[60] W. Taifan, A.A. Arvidsson, E. Nelson, A. Hellman, J. Baltrusaitis, CH_4 and H_2S reforming to CH_3SH and H_2 catalyzed by metal-promoted Mo_6S_8 clusters: a first-principles micro-kinetic study, Catal. Sci. Technol. 7 (2017) 3546–3554.

[61] S. Wang, S.Y. Li, L. Zhang, Z.F. Qin, Y.Y. Chen, M. Dong, J.F. Li, W.B. Fan, J.G. Wang, Mechanistic insights into the catalytic role of various acid sites on ZSM-5 zeolite in the carbonylation of methanol and dimethyl ether, Catal. Sci. Technol. 8 (2018) 3193–3204.

[62] K.A. Goulas, Y.Y. Song, G.R. Johnson, J.P. Chen, A.A. Gokhale, L.C. Grabow, F.D. Toste, Selectivity tuning over monometallic and bimetallic dehydrogenation catalysts: effects of support and particle size, Catal. Sci. Technol. 8 (2018) 314–327.

[63] D. Wang, J. Jiang, H.F. Wang, P. Hu, Revealing the volcano-shaped activity trend of triiodide reduction reaction: a DFT study coupled with microkinetic analysis, ACS Catal. 6 (2016) 733–741.

[64] Z.J. Chen, Y. Mao, J.F. Chen, H.F. Wang, Y.D. Li, P. Hu, Understanding the dual active sites of the FeO/Pt(111) interface and reaction kinetics: density functional theory study on methanol oxidation to formaldehyde, ACS Catal. 7 (2017) 4281–4290.

[65] H.Y. Yuan, J.F. Chen, Y.L. Guo, H.F. Wang, P. Hu, Insight into the superior catalytic activity of MnO_2 for low-content NO oxidation at room temperature, J. Phys. Chem. C 122 (2018) 25365–25373.

[66] J. Zhang, H.M. Jin, M.B. Sullivan, F.C.H. Lim, P. Wu, Study of Pd-Au bimetallic catalysts for CO oxidation reaction by DFT calculations, Phys. Chem. Chem. Phys. 11 (2009) 1441–1446.

[67] C. Fan, Y.A. Zhu, Y. Xu, Y. Zhou, X.G. Zhou, D. Chen, Origin of synergistic effect over Ni-based bimetallic surfaces: a density functional theory study, J. Chem. Phys. 137 (2012) 014703-1-10.

[68] B. Hwang, H. Kwon, J. Ko, B.K. Kim, J.W. Han, Density functional theory study for the enhanced sulfur tolerance of Ni catalysts by surface alloying, Appl. Surf. Sci. 429 (2018) 87–94.

[69] M.C. Luo, S.J. Guo, Strain-controlled electrocatalysis on multimetallic nanomaterials, Nat. Rev. Mater. 2 (2013) 17059-1-13.

[70] A. Hussain, Beneficial effect of Cu on a Cu-modified Au catalytic surface for CO oxidation reaction: a DFT study, J. Phys. Chem. C 117 (2013) 5084–5094.

[71] Q.Y. Yuan, H.A. Doan, L.C. Grabow, S.R. Brankovic, Finite size effects in submonolayer catalysts investigated by CO electrosorption on Pt_{sML}/Pd(100), J. Am. Chem. Soc. 139 (2017) 13676–13679.

[72] H. Thirumalai, J.R. Kitchin, Investigating the reactivity of single atom alloys using density functional theory, Top. Catal. 61 (2018) 462–474.

[73] Y.C. Huang, J.Y. Du, C.Y. Ling, T. Zhou, S.F. Wang, Methane dehydrogenation on Au/Ni surface alloys-a first-principles study, Catal. Sci. Technol. 3 (2013) 1343–1354.

[74] Y.C. Huang, C.Y. Ling, M. Jin, J.Y. Du, T. Zhou, S.F. Wang, Water adsorption and dissociation on Ni surface: effects of steps, dopants, coverage and self-aggregation, Phys. Chem. Chem. Phys. 15 (2013) 17804–17817.

[75] J.R. Kitchin, J.K. Nørskov, M.A. Barteau, J.G. Chen, Role of strain and ligand effects in the modification of the electronic and chemical properties of bimetallic surfaces, Phys. Rev. Lett. 93 (2004) 156801-1-4.
[76] G. Kresse, J. Furthmüller, Efficiency of ab-initio total energy calculations for metals and semiconductors using a plane-wave basis set, Comput. Mater. Sci. 6 (1996) 15–50.
[77] G. Kresse, J. Furthmüller, Efficient iterative schemes for ab initio total-energy calculations using a plane-wave basis set, Phys. Rev. B: Condens. Matter Mater. Phys. 54 (1996) 11169–11186.
[78] G. Kresse, J. Hafner, Ab initio molecular-dynamics simulation of the liquid-metal amorphous-semiconductor transition in germanium, Phys. Rev. B: Condens. Matter Mater. Phys. 49 (1994) 14251–14269.
[79] M. Gajdoš, K. Hummer, G. Kresse, J. Furthmüller, F. Bechstedt, Linear optical properties in the projector-augmented wave methodology, Phys. Rev. B 73 (2006) 045112-1-9.
[80] P.E. Blöchl, Projector augmented-wave method, Phys. Rev. B 50 (1994) 17953–17979.
[81] J.J. Mortensen, L.B. Hansen, K.W. Jacobsen, Real-space grid implementation of the projector augmented wave method, Phys. Rev. B 71 (2005) 035109-1-11.
[82] M. Ernzerhof, J.P. Perdew, Generalized gradient approximation to the angle- and system-averaged exchange hole, Phys. Rev. Lett. 109 (1998) 3313–3320.
[83] G. Henkelman, B.P. Uberuaga, H. Jónsson, A climbing image nudged elastic band method for finding saddle points and minimum energy paths, J. Chem. Phys. 113 (2000) 9901–9904.
[84] G. Henkelman, H. Jónsson, Improved tangent estimate in the nudged elastic band method for finding minimum energy paths and saddle points, J. Chem. Phys. 113 (2000) 9978–9985.
[85] G. Henkelman, H. Jónsson, A dimer method for finding saddle points on high dimensional potential surfaces using only first derivatives, J. Chem. Phys. 111 (1999) 7010–7022.
[86] P.H. Xiao, D. Sheppard, J. Rogal, G. Henkelman, Solid-state dimer method for calculating solid-solid phase transitions, J. Chem. Phys. 140 (2014) 174104-1-6.
[87] J.P. Clay, J.P. Greeley, F.H. Ribeiro, W.N. Delgass, W.F. Schneider, DFT comparison of intrinsic WGS kinetics over Pd and Pt, J. Catal. 320 (2014) 106–117.
[88] J. Häglund, A.F. Guillermet, G. Grimvall, M. Körling, Theory of bonding in transition-metal carbides and nitrides, Phys. Rev. B: Condens. Matter Mater. Phys. 48 (1993) 11685–11691.
[89] H.M. Otte, Lattice parameter determinations with an X-ray spectrogoniometer by the Debye-Scherrer method and the effect of specimen condition, J. Appl. Phys. 32 (1961) 1536–1546.
[90] K. Li, H.Y. Liu, R.G. Zhang, L.X. Ling, B.J. Wang, Interaction between bimetal cluster Ni_2Co_2 and MgO and its effect on H adsorption and H_2 dissociation: a DFT study, Appl. Surf. Sci. 390 (2016) 7–16.
[91] Y.T. Cao, L.X. Ling, H. Lin, M.H. Fan, P. Liu, R.G. Zhang, B.J. Wang, DFT study on CO oxidative coupling to DMO over Pd_4/TiO_2 and Pd_4/TiO_2-Ov: a role of oxygen vacancy on support, Comput. Mater. Sci. 159 (2019) 1–11.
[92] D. Jiang, S. Dai, The role of low-coordinate oxygen on Co_3O_4(110) in catalytic CO oxidation, Phys. Chem. Chem. Phys. 13 (2011) 978–984.
[93] Q. Li, R. García-Muelas, N. López, Microkinetics of alcohol reforming for H_2 production from a FAIR density functional theory database, Nat. Commun. 9 (2018) 526-1-8.
[94] Y.M. Choi, P. Liu, Mechanism of ethanol synthesis from syngas on Rh(111), J. Am. Chem. Soc. 131 (2009) 13054–13061.
[95] Q.L. Tang, S.R. Zhang, Y.P. Liang, Influence of step defects on the H_2S splitting on copper surfaces from first-principles microkinetic modeling, J. Phys. Chem. C 116 (2012) 20321–20331.
[96] H. Wang, C.Z. He, L.Y. Huai, F.M. Tao, J.Y. Liu, Decomposition of methanol on clean and oxygen-predosed V(100): a first-principles study, J. Phys. Chem. C 116 (2012) 25344–25353.
[97] X.M. Cao, R. Burch, C. Hardacre, P. Hu, An understanding of chemoselective hydrogenation on crotonaldehyde over Pt(111) in the free energy landscape: the microkinetics study based on first-principles calculations, Catal. Today 165 (2011) 71–79.
[98] F. He, K. Li, G.U. Xie, Y. Wang, M.G. Jiao, H. Tang, Z.J. Wu, Understanding the enhanced catalytic activity of Cu1@Pd3(111) in formic acid dissociation, a theoretical perspective, J. Power Sources 316 (2016) 8–16.